Politecnico di Torino

Porto Institutional Repository

[Article] Nonlinear mitigation on subcarrier-multiplexed PM-16QAM optical systems

(Article begins on next page)
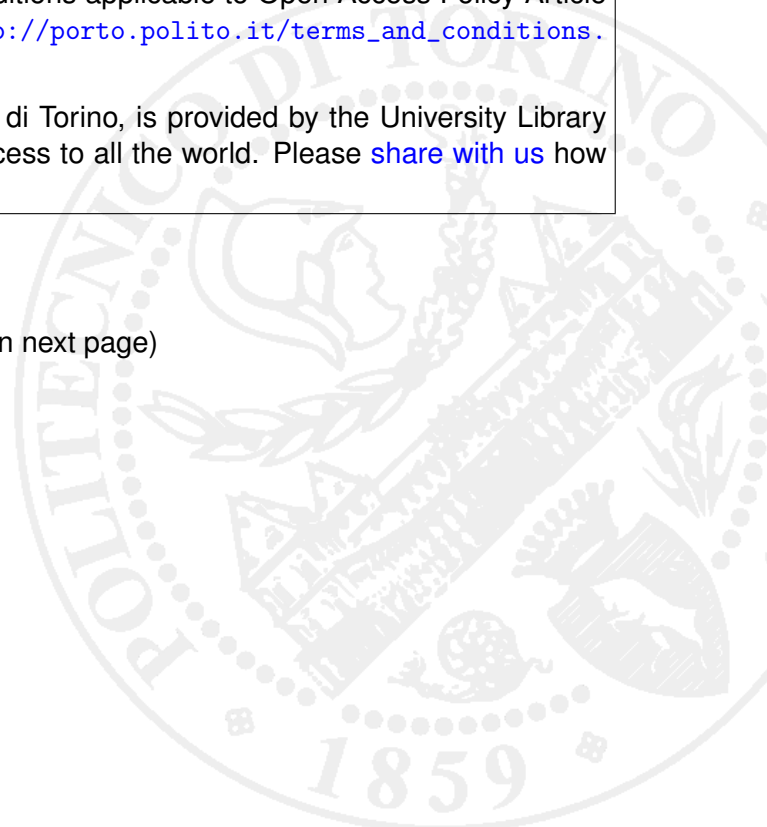
Nonlinear mitigation on subcarrier-multiplexed PM-16QAM optical systems

F. P. GUIOMAR,[1,*] A. CARENA,[1] G. BOSCO,[1] L. BERTIGNONO,[1] A. NESPOLA,[2] AND P. POGGIOLINI[1]

[1] *DET, Politecnico di Torino, Corso Duca degli Abruzzi, 24, 10129, Torino, Italy*
[2] *Istituto Superiore Mario Boella, via Pier Carlo Boggio 61, 10138 Torino, Italy*
[*] *fernando.guiomar@polito.it*

Abstract: We report a comprehensive set of experimental, simulation and analytical results on the benefit of nonlinear mitigation strategies for multi-subcarrier (MSC) PM-16QAM transmission systems. First, we demonstrate ~9% maximum reach gain enabled by symbol-rate optimization (SRO) of MSC-PM-16QAM in a 31 channels WDM transmission experiment. Then, we demonstrate that, in the considered experimental scenario, the gain provided by digital backpropagation (DBP) over single-carrier (SC) transmission is similar to that achieved by SRO over MSC transmission. Furthermore, we show that the SRO phenomenon can be weakened after self-channel interference (SCI) removal through DBP. As a result, and due to DBP performance limitations in the experiment, the combined effect of SRO and DBP was found to enable only an additional 4% gain in maximum reach. Finally, we address the impact and symbol-rate dependence of nonlinear phase noise (NLPN) in MSC-PM-16QAM transmission, discussing on the NLPN mitigation capability of standard carrier phase estimation (CPE) and on respective gains that could be achieved through its enhanced mitigation.

OCIS codes: (060.2360) Fiber optics links and subsystems; (060.1660) Coherent communications.

References and links

1. M. Qiu, Q. Zhuge, X. Xu, M. Chagnon, M. Morsy-Osman, and D. V. Plant, "Subcarrier multiplexing using DACs for fiber nonlinearity mitigation in coherent optical communication systems," in *Proc. Optical Fiber Communication Conf. and Exposition (OFC),* (2014), Tu3J.2.
2. M. Qiu, Q. Zhuge, M. Chagnon, Y. Gao, X. Xu, M. Morsy-Osman, and D. V. Plant, "Digital subcarrier multiplexing for fiber nonlinearity mitigation in coherent optical communication systems," Opt. Express **22**, 18770–18777 (2014).
3. N. Rossi, P. Serena, and A. Bononi, "Symbol-rate dependence of dominant nonlinearity and reach in coherent WDM links," J. Lightwave Technol. **33**, 3132–3143 (2015).
4. H. Nakashima, T. Tanimura, T. Oyama, Y. Akiyama, T. Hoshida, and J. C. Rasmussen, "Experimental investigation on nonlinear tolerance of subcarrier multiplexed signals with spectrum optimization," in *Proc. 41th European Conference on Optical Communication (ECOC),* (2015), ID: 0391.
5. A. Nespola, L. Bertignono, G. Bosco, A. Carena, Y. Jiang, S. M. Bilal, P. Poggiolini, S. Abrate, and F. Forghieri, "Experimental demonstration of fiber nonlinearity mitigation in a WDM multi-subcarrier coherent optical system," in *Proc. 41th European Conference and Exhibition on Optical Communication (ECOC),* (2015), ID: 0382.
6. P. Poggiolini, A. Nespola, Y. Jiang, G. Bosco, A. Carena, L. Bertignono, S. M. Bilal, S. Abrate, and F. Forghieri, "Analytical and experimental results on system maximum reach increase through symbol rate optimization," J. Lightwave Technol. **34**, 1872–1885 (2016).
7. J. X. Cai, M. Mazurczyk, O. V. Sinkin, M. Bolshtyansky, D. G. Foursa, and A. Pilipetskii, "Experimental study of subcarrier multiplexing benefit in 74 nm bandwidth transmission up to 20,450 km," in *Proc. European Conference on Optical Communication (ECOC),* (2016), pp. 677–679.
8. F. Buchali, W. Idler, K. Schuh, L. Schmalen, T. Eriksson, G. Bôcherer, P. Schulte, and F. Steiner, "Study of electrical subband multiplexing at 54 GHz modulation bandwidth for 16QAM and probabilistically shaped 64QAM," in *Proc. European Conference on Optical Communication (ECOC),* (2016), pp. 49–51.
9. G. Bosco, S. M. Bilal, A. Nespola, P. Poggiolini, and F. Forghieri, "Impact of the transmitter IQ-skew in multi-subcarrier coherent optical systems," in *Proc. Optical Fiber Communication Conf. and Exposition (OFC),* (2016), W4A.5.
10. S. M. Bilal, C. Fludger, and G. Bosco, "Carrier phase estimation in multi-subcarrier coherent optical systems," IEEE Photonics Technol. Lett. **28**, 2090–2093 (2016).
11. J. Fickers, A. Ghazisaeidi, M. Salsi, G. Charlet, P. Emplit, and F. Horlin, "Multicarrier offset-QAM for long-haul coherent optical communications," J. Lightwave Technol. **32**, 4069–4076 (2014).

12. A. C. Meseguer, J. Renaudier, R. Rios-Müller, P. Tran, and G. Charlet, "Impact of bandwidth efficiency in nonlinear tolerance of multicarrier modulations," J. Lightwave Technol. **34**, 1787–1792 (2016).

13. A. Carbó, J. Renaudier, P. Tran, and G. Charlet, "Experimental analysis of non linear tolerance dependency of multicarrier modulations versus number of WDM channels," in *Proc. Optical Fiber Communications Conference and Exhibition (OFC),* (2016), Tu3A.6.

14. R. Dar, M. Feder, A. Mecozzi, and M. Shtaif, "Properties of nonlinear noise in long, dispersion-uncompensated fiber links," Opt. Express **21**, 25685–25699 (2013).

15. A. Carena, G. Bosco, V. Curri, Y. Jiang, P. Poggiolini, and F. Forghieri, "EGN model of non-linear fiber propagation," Opt. Express **22**, 16335–16362 (2014).

16. L. Galdino, G. Liga, G. Saavedra, D. Ives, R. Maher, A. Alvarado, S. Savory, R. Killey, and P. Bayvel, "Experimental demonstration of modulation-dependent nonlinear interference in optical fibre communication," in *Proc. European Conf. Optical Communication (ECOC),* (2016), pp. 950–952.

17. M. Secondini and E. Forestieri, "Analytical fiber-optic channel model in the presence of cross-phase modulation," IEEE Photonics Technol. Lett. **24**, 2016–2019 (2012).

18. R. Dar, M. Feder, A. Mecozzi, and M. Shtaif, "Inter-channel nonlinear interference noise in WDM systems: Modeling and mitigation," J. Lightwave Technol. **33**, 1044–1053 (2015).

19. A. Nespola, L. Bertignono, G. Bosco, A. Carena, P. Poggiolini, and F. Forghieri, "Independence of the impact of inter-channel non-linear effects on modulation format and system implications," in *Proc. European Conference on Optical Communication (ECOC),* (2016), pp. 485–487.

20. E. Ip and J. M. Kahn, "Compensation of dispersion and nonlinear impairments using digital backpropagation," J. Lightwave Technol. **26**, 3416–3425 (2008).

21. P. Poggiolini, G. Bosco, A. Carena, V. Curri, Y. Jiang, and F. Forghieri, "The GN-model of fiber non-linear propagation and its applications," J. Lightwave Technol. **32**, 694–721 (2014).

22. R. Dar and P. J. Winzer, "On the limits of digital back-propagation in fully loaded WDM systems," IEEE Photonics Technol. Lett. **28**, 1253–1256 (2016).

23. A. Nespola, Y. Jiang, L. Bertignono, G. Bosco, A. Carena, S. M. Bilal, P. Poggiolini, and F. Forghieri, "Effectiveness of digital back-propagation and symbol-rate optimization in coherent WDM optical systems," in *Proc. Optical Fiber Communication Conf. and Exposition (OFC),* (2016), Th3D.2.

24. F. P. Guiomar, A. Carena, G. Bosco, L. Bertignono, A. Nespola, and P. Poggiolini, "Effectiveness of symbol-rate optimization with PM-16QAM subcarriers in WDM transmission," in *submitted to Optical Fiber Conference (OFC),* (2017).

25. R. Rios-Muller, J. Renaudier, and G. Charlet, "Blind receiver skew compensation and estimation for long-haul non-dispersion managed systems using adaptive equalizer," J. Lightwave Technol. **33**, 1315–1318 (2015).

26. I. Fatadin, D. Ives, and S. J. Savory, "Laser linewidth tolerance for 16-QAM coherent optical systems using QPSK partitioning," IEEE Photon. Technol. Lett. **22**, 631–633 (2010).

27. A. Bisplinghoff, C. Vogel, T. Kupfer, S. Langenbach, and B. Schmauss, "Slip-reduced carrier phase estimation for coherent transmission in the presence of non-linear phase noise," in *Proc. Optical Fiber Communication Conference (OFC),* (2013), OTu3I.1.

28. P. Poggiolini, A. Carena, Y. Jiang, G. Bosco, V. Curri, and F. Forghieri, "Impact of low-OSNR operation on the performance of advanced coherent optical transmission systems," in *Proc. European Conference on Optical Communication (ECOC),* (2014), Mo.4.3.2.

29. T. Pfau, S. Hoffmann, and R. Noé, "Hardware-efficient coherent digital receiver concept with feedforward carrier recovery for M-QAM constellations," J. Lightw. Technol. **27**, 989–999 (2009).

30. X. Zhou, "An improved feed-forward carrier recovery algorithm for coherent receivers with M-QAM modulation format," IEEE Photon. Technol. Lett. **22**, 1051–1053 (2010).

1. Introduction

The use of multi-subcarrier (MSC) signals has been recently emerging as an alternative optical transmission technique for the widely deployed single-carrier (SC) systems. It exploits the flexibility on signal design provided by fast digital-to-analog converters (DACs), enabling to create multiple electrically-generated subcarrier signals composed of an adjustable number of low symbol-rate tributaries. The main competitive advantage of MSC over standard SC transmission lies on the additional nonlinear robustness provided by the recently identified symbol-rate optimization (SRO) phenomenon [1–8]. Exploring the additional degree of freedom (number of subcarriers) provided by MSC transmission, several analytical, simulation and experimental works have identified that the total nonlinear interference (NLI) impinging on a given channel under test (CUT) turns out to depend on the per-subcarrier symbol-rate [1–8]. Indeed, the optimum symbol-rate that minimizes NLI was found to be in the range of 2–10 GBaud for typical uncompensated optical fiber links [6].

SRO has been firstly identified in the pioneer experimental work of [1], where ~22% extended reach has been found by transmitting a single-channel 24 GBaud PM-QPSK in the form of 8×3 GBaud subcarriers. Other PM-QPSK-based experiments have followed, proving the existence of SRO also in WDM transmission. A 19×128 Gb/s PM-QPSK experiment has been reported in [5], where 12% extended reach was found with an 8-subcarrier channel configuration. In [4], enhanced SRO benefits were found by increasing the inter-subcarrier spacing in a 8-channel PM-QPSK experiment, yielding 0.7 dB gain in required OSNR after propagation, even suffering from a 0.3 dB back-to-back (B2B) MSC implementation penalty. Indeed, increased MSC B2B penalties relatively to SC transmission have been reported in several recent works. These penalties can be caused by limitations on the electronic transmission and processing of MSC signals composed of low symbol-rate subcarriers. The skew between in-phase (I) and quadrature (Q) components at the transmitter side has been identified as a critical performance limiting aspect for MSC transmission, requiring dedicated adaptive filter structures for its compensation [9]. In addition, the performance of standard carrier phase estimation (CPE) is known to be dependent on the characteristic linewidth times symbol-duration product. As a consequence, advanced CPE schemes may be required to avoid MSC implementation penalties at low symbol-rate transmission [10]. The excess B2B penalty coming from MSC implementation at low symbol-rates can be a key limiting factor, reducing the observed SRO or even resulting in degraded performance [11–13].

After the demonstration of SRO over MSC-PM-QPSK systems, the technical discussion has moved towards the modulation format dependence of NLI [14–16], and its possible implications on the SRO benefits with higher-order QAM subcarriers. Due to a more Gaussian-like geometric distribution of symbols, higher-order QAM constellations tend to suffer from enhanced NLI generation. This NLI format dependence is already taken into account by advanced analytical models, such as the enhanced Gaussian noise (EGN) model [14, 15], which includes NLI correction factors based on the transmitted signal constellation. In order to assess the impact of NLI format dependence on the SRO benefit achievable with PM-16QAM subcarriers, several experiments have been recently performed [2, 7, 8]. A maximum reach increase of 8-14% has been demonstrated in the single-channel experiments of [2] and [8]. In [7], the achievable SRO with PM-QPSK and PM-16QAM subcarriers has been assessed in a C+L WDM experiment. While a gain of 0.8 dB in Q-factor was found by optimizing the symbol-rate of MSC-PM-QPSK, a more modest improvement was found with PM-16QAM (0.2 dB) .

Recently, it has been shown that the NLI format dependence mostly manifests itself in the form of long-correlated nonlinear phase noise (NLPN) [17–19], which increases the phase variance of the received constellation symbols. Nevertheless, this NLPN phenomenon is characterized by long-term time correlations, opening up the possibility of its mitigation through CPE. The full potential of SRO in MSC transmission with high-order QAM subcarriers may then be unlocked by an efficient mitigation of NLPN. On the other hand, digital backpropagation (DBP) has been the method of choice for single channel interference (SCI) removal [20] in long-haul optical transmission systems. Its performance limits in terms of maximum reach gain in fully-loaded WDM transmission have been estimated to be in the range of 10-25% [21, 22]. SRO and DBP can also be combined together to maximize nonlinear mitigation, as already demonstrated in [23], expanding the MSC-PM-QPSK results of [5] to show an additional 8% reach increase provided by DBP, on top of the baseline 12% enabled by SRO, totalling 20% extended reach over SC transmission.

However, the overall performance enhancement achievable by nonlinear mitigation through SRO, DBP and/or NLPN removal still remains unclear. In practical terms, it is important to answer the following question. Which nonlinear phenomena should we target and which mitigation techniques are more appropriate for symbol-rate optimized MSC transmission systems?

In this paper, extending the work of [24], we report a 31-channel WDM experimental campaign
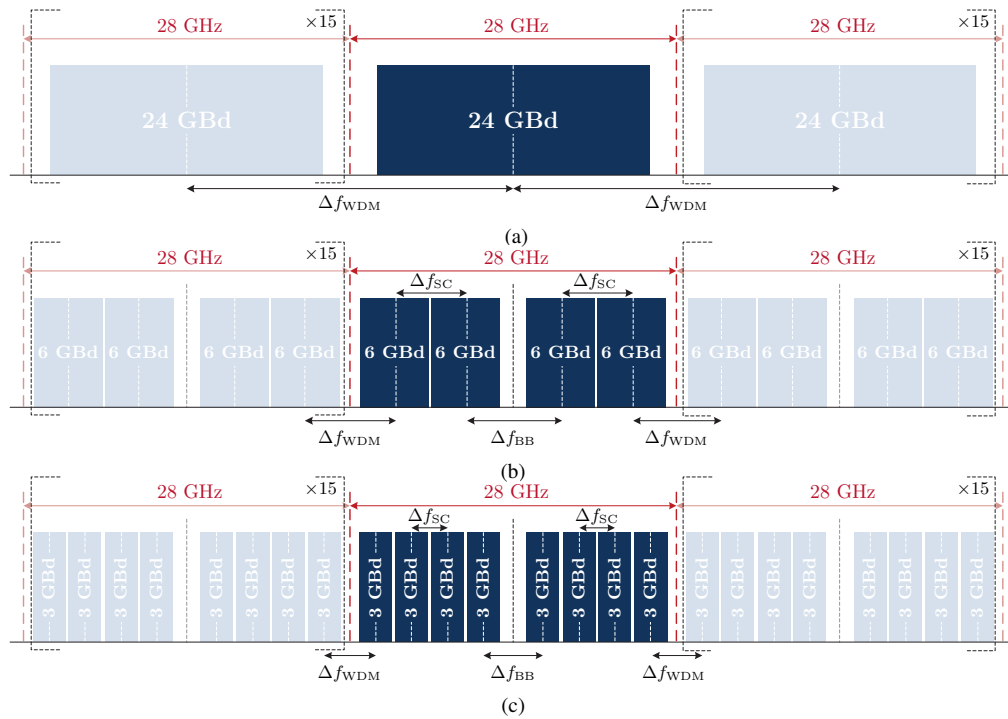
Fig. 1. Spectra schematic representation of 31-channel WDM-MSC transmission adopted in this work. The given examples correspond to a) 1×24 GBaud, b) 6×4 GBaud, and c) 8×3 GBaud.

on MSC-PM-16QAM transmission, with comprehensive symbol-rate optimization, starting from a baseline SC configuration of 1×24 GBaud down to a MSC setup with 12×2 GBaud. We assess the maximum reach gain provided by SRO in the experimental scenario, and we confirm its validity by comparison with analytical (EGN model) and simulation (split-step based) results. After SCI mitigation through DBP, we report on the combined benefit of SRO + DBP, and we discuss on the maximum performance limits of such a strategy. Finally, we assess the impact of NLPN in our system by analyzing the phase variance of the output constellation, and we discuss on the potential benefits coming from its enhanced mitigation employing an ideal fully data-aided CPE.

2. MSC configuration and experimental setup

The MSC configurations to be studied in this work are described in Table 1 and illustrated in Fig. 1 for the exemplary cases of 1×24 GBaud, 4×6 GBaud and 8×3 GBaud. In all cases, we consider 31 co-propagating channels, each of which designed according to one of the adopted MSC configurations detailed in Table 1. The channel under test is placed in the middle of the spectrum, centered at a wavelength of 1557.6 nm. The inter-channel spacing is fixed at 28 GHz. We start with the baseline case of SC transmission at 24 GBaud. That will be our benchmark configuration, against which we will study the added benefit provided by SRO. Then, we have tested all other MSC configurations with symbol-rates that are divisors of 24, down to 12×2 GBaud. Note that, we skipped the 3×8 GBaud configuration to avoid placing one subcarrier at the baseband. The reason for this choice has to do with "M" shape performance experienced by MSC signals, due to increased B2B penalty both in the lower- and higher-frequency subcarriers, as already reported in other works [7]. This behavior is likely
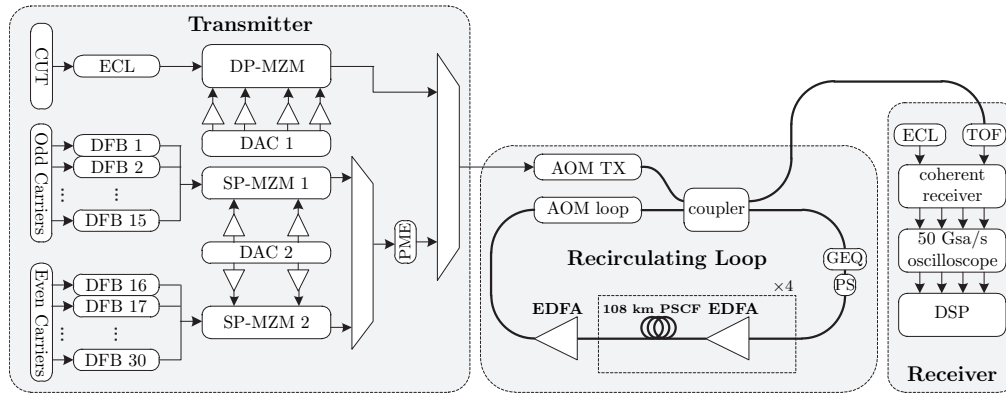
Fig. 2. Laboratorial setup of the 31-channel MSC transmission experiment.

caused by an enhanced low-frequency noise associated with the DAC and electrical drivers on the generation of the signal. To reduce the impact of this low-frequency noise, we have decided to insert a frequency gap of 1 GHz between baseband and the nearest subcarrier, as depicted in Fig. 1. As a result, the two central subcarriers in each channel have a larger frequency separation, Δf_{BB}, than the remaining ones, which are separated by $\Delta f_{\text{SC}} = (1 + \alpha) \times R_s$, where R_s is the symbol-rate per subcarrier and $\alpha = 0.05$ is the roll-off factor of the root-raised-cosine pulse shaping filter. Note that for the 2×12 GBaud configuration, all subcarriers in the overall WDM comb become evenly spaced by 14 GHz. All details of frequency separation between subcarriers are listed in Table 1, together with the length of the periodic sequence (in symbols) loaded in the DAC, which was defined according to the DAC memory, while simultaneously ensuring phase continuity between sequence repetitions.

The experimental setup of the 31-channel MSC experiment is shown in Fig. 2. At the transmitter side, all subcarriers are pulse shaped (roll-off 0.05) and pre-emphasized to compensate for the bandwidth limitation of the 64 GSa/s DAC. The central channel, the CUT, is generated by an external cavity laser (ECL) with <100 kHz linewidth and modulated by a dual-polarization Mach-Zehnder modulator (MZM). In turn, the remaining 30 interfering channels are generated by distributed-feedback (DFB) lasers and modulated (separately for even and odd channels) by a single-polarization MZM followed by a polarization multiplexing emulator (PME).

The recirculating loop is composed of 4 spans of pure silica core fiber (PSCF) with average length of 108 km, dispersion parameter of 20.12 ps/(nm·km) and attenuation coefficient of 0.162 dB/km. The total span loss, including all insertion losses, is 18.75 dB. We use EDFA-

Table 1. Description of the adopted MSC configurations. R_s – symbol-rate (in GBaud); N_{SC} – number of subcarriers; Δf_{SC} – frequency separation between subcarriers (in GHz); Δf_{BB} – frequency separation between the two subcarriers nearest to baseband (in GHz); Δf_{WDM} – frequency separation between edge subcarriers from different channels (in GHz); N_{syms} – periodic sequence length in symbols.

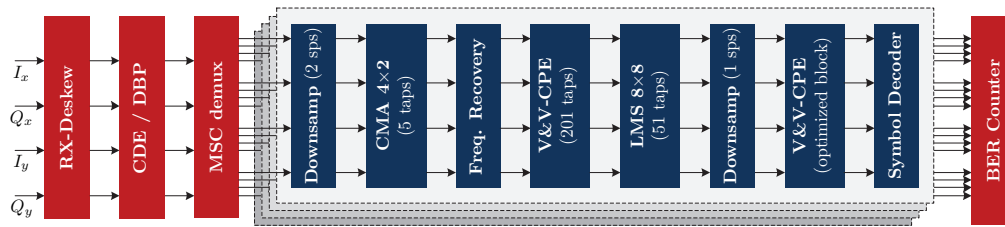| R_s	N_{SC}	Δf_{SC}	Δf_{BB}	Δf_{WDM}	N_{syms}
24	1	–	–	28	$2^{15} - 8$
12	2	14	14	14	$2^{13} - 8$
6	4	6.3	8.3	7.1	$2^{11} - 8$
4	6	4.2	6.2	5	$2^{11} - 8$
3	8	3.15	5.15	3.95	$2^{11} - 8$
2	12	2.1	4.1	2.9	$2^{11} - 8$

Fig. 3. Sequence of DSP algorithms utilized for the processing of the received MSC signals.

only amplification (fixed-gain that inverts the span attenuation and noise figure of 5.2 dB) and a spectrally-resolved gain equalizer (GEQ) to compensate for the EDFA gain-tilt and ripples. Finally, a loop synchronized polarization scrambler is used to statistically average the polarization effects.

At the receiver, the CUT is filtered by a tunable optical filter (TOF) and mixed with an ECL (<100 kHz). Finally, the coherently detected signal is sampled by a 50 GSa/s real-time oscilloscope (Tektronix DPO73304DX).

3. DSP subsystems and B2B performance

The set of DSP algorithms applied for the processing of the received MSC signals is shown in Fig. 3.

First, the temporal IQ skew created by the coherent receiver in the *x* and *y* polarizations is estimated and removed. This skew is created by slight mismatches on the lengths of the electrical cables at the receiver, and it remained fixed over the time of the experiment. Static equalization is then performed over the entire MSC signal, employing either chromatic dispersion equalization (CDE) or digital backpropagation (DBP). DBP is applied employing a standard split-step Fourier method [20] with 4 steps per span. At this point the MSC signal is ready for digital demultiplexing of its subcarrier components, which are filtered and converted to baseband. After downsampling to 2 samples per symbol (SpS), the residual receiver skew is compensated by a 4×2 constant modulus algorithm (CMA)-driven equalizer [25] with 5 taps. The frequency offset due to intradyne detection is removed with a sliding-window spectral method. Then, a first coarse estimation of the carrier phase is performed using the 16QAM-modified (QPSK partitioning) Viterbi & Viterbi (V&V) algorithm [26] with long block length (201 taps). To avoid the increased cycle-slip probability incurred by the use of short CPE block lengths, we
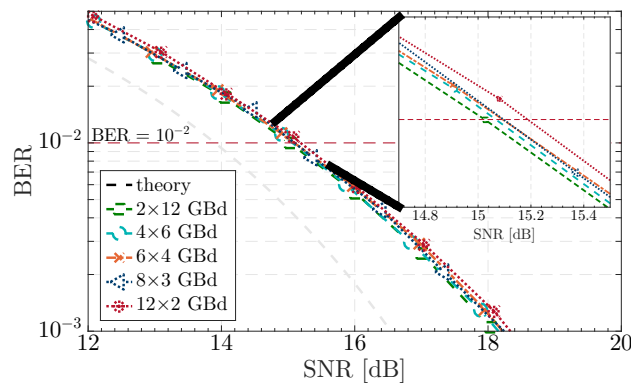

Fig. 4. Optical B2B characterization of the MSC transmission system.

have adopted the dual-branch CPE approach proposed in [27], applying an additional V&V CPE with long block length (101 taps) in parallel with the optimized block length CPE. This allows to effectively detect and correct possible cycle-slips incurred by the shorter block length CPE, as demonstrated in [27]. Note that, although this first CPE stage operates over a signal with 2 samples per symbol, the phase estimation operation is actually only performed over 1 of the 2 available samples (best sampling instant determined in the previous CMA filtering stage). The estimated phase noise trace is then upsampled to 2 samples per symbol and removed from the input signal. Also note that the use of 2 samples per symbol at this stage is beneficial for the subsequent adaptive linear equalization, whose maximum performance requires sampling at the Nyquist rate. In [9], it was shown the IQ skew at the transmitter side can have a severe impact on MSC transmission, causing a performance degradation that is more severe for the subcarriers located at higher frequencies. Therefore, in order to avoid the degraded SNR at high frequencies that would hinder the subcarrier demodulation required by CPE, in this first stage the carrier phase is only estimated over one of the central subcarriers (where IQ skew produces small impact), with the extracted phase correction being then applied to the remaining subcarriers. The removal of laser phase noise in the first CPE stage enables the subsequent use of a bank of 8 × 8 real-valued adaptive equalizers for the compensation of the transmitter IQ skew [9]. Each equalizer is 8 × 8 because it operates on pairs of subcarriers symmetric with respect to the channel center frequency. This 8×8 adaptive filter is set to operate with 51 taps, whose values are updated according to a least mean squares (LMS) criteria, initialized in data-aided mode for tap convergence and then switched to decision-directed mode. To fine tune phase estimation, a second V&V CPE stage is applied after downsampling to 1 SpS. Aiming at maximizing the NLPN mitigation, this second CPE operates independently over each subcarrier with an optimized block length. Finally, the received symbols are decoded and the BER per subcarrier is counted. The adopted metric for system performance is the average BER among all subcarriers.

The optical B2B performance of the different MSC configurations under study is shown in Fig. 4. All MSC configurations down to 3 GBaud per subcarrier operate with a B2B penalty of ∼ 1.1 ± 0.1 dB relatively to the theoretical limit at a target BER of 10^{-2}. The exception is the 12×2 GBaud case, whose best B2B performance was found at ∼1.3 dB of B2B penalty. We attribute this extra penalty experienced at 2 GBaud to the limited CPE tolerance towards the linewidth times symbol duration product.

4. Nonlinear mitigation via SRO and/or DBP

We initiate our signal propagation analysis by plotting in Fig. 5 the power spectral density of NLI, G_{NLI}, for all considered MSC configurations, at a fixed power per channel of 0 dBm. These results were obtained by the EGN model [15] with PM-16QAM correction factors (EGN-16QAM) to account for the modulation format dependency of NLI. The impact of the defined frequency spacing on the produced NLI per subcarrier is well visible in Fig. 5. Indeed, at low symbol-rate, there is a fluctuation of ∼0.5 dB in the total NLI power between subcarriers, which may translate into slightly different individual reaches. Since we are interested in analyzing the maximum reach of the system based on the average BER among all subcarriers, from now on, our EGN results in terms of maximum reach are obtained as follows:

- The total NLI power per subcarrier, P_{NLI} (in W), is determined through the EGN, by integrating the traces shown in Fig. 5 individually over each subcarrier bandwidth;

- The corresponding per-subcarrier SNR (in dB) is determined as,

$$\text{SNR} = 10 \log_{10} \left(\frac{P_{tx} - P_{NLI}}{P_{ASE} + P_{NLI}} \right), \tag{1}$$

where P_{tx} is the transmitted power per subcarrier (in W) and P_{ASE} is the ASE noise

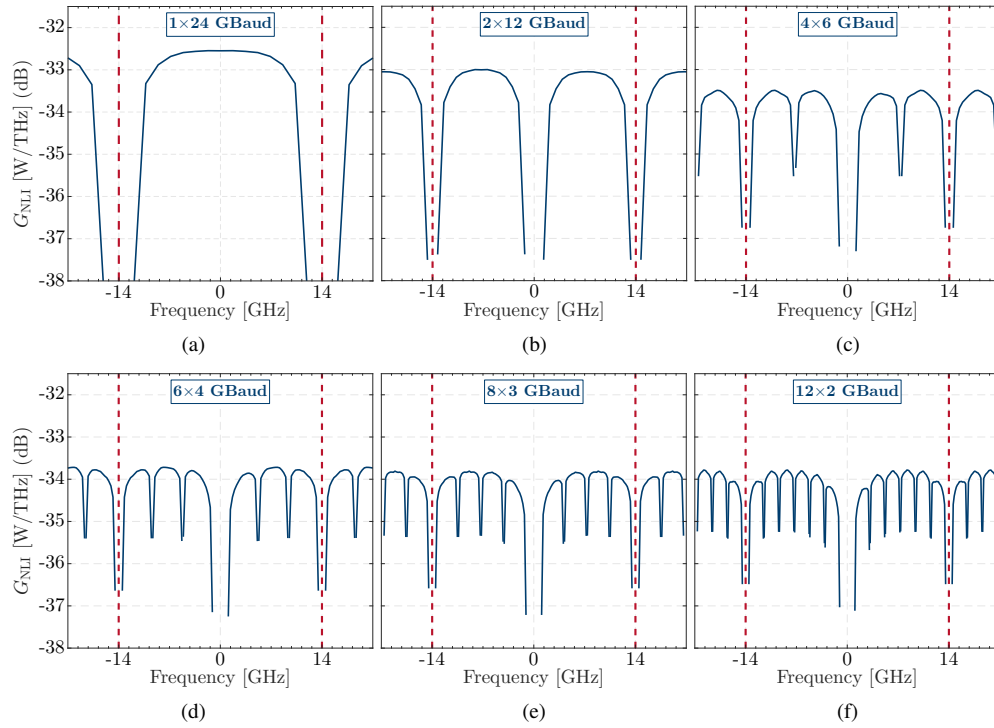Fig. 5. Power spectral density of NLI at a fixed transmitted power of 0 dBm per channel. a) 1×24 GBaud, b) 2×12 GBaud, c) 4×6 GBaud, d) 6×4 GBaud, e) 8×3 GBaud, f) 12×2 GBaud.

power measured over the subcarrier bandwidth (in W). The subtraction of P_{NLI} from the numerator of (1) is intended to provide an heuristic correction for nonlinear signal power depletion [28].

- Each per-subcarrier SNR is converted into BER as

$$\mathrm{BER} = \frac{3}{8}\mathrm{erfc}\left(\sqrt{\frac{10^{\frac{\mathrm{SNR}}{10}}}{10}}\right), \tag{2}$$

where erfc is the complementary error function.

- The average BER is then calculated from all individual BERs corresponding to each subcarrier, and converted back to an equivalent SNR;

- The procedure is repeated for different transmitted powers and propagation lengths;

- Setting a limit BER, $\mathrm{BER}_{\mathrm{max}} = 10^{-2}$, and accounting for the B2B penalty, $\mathrm{B2B}_{\mathrm{pen}}$ (in dB), the limit SNR, $\mathrm{SNR}_{\mathrm{max}}$ (in dB), for system operation is calculated as,

$$\mathrm{SNR}_{\mathrm{max}} = 10\log_{10}\left[10\left(\mathrm{erfc}^{-1}\left(\frac{8}{3}\mathrm{BER}_{\mathrm{max}}\right)\right)^2\right] + \mathrm{B2B}_{\mathrm{pen}}. \tag{3}$$

- Finally, the system maximum reach is determined by linear interpolation of the obtained SNR values around $\mathrm{SNR}_{\mathrm{max}}$.
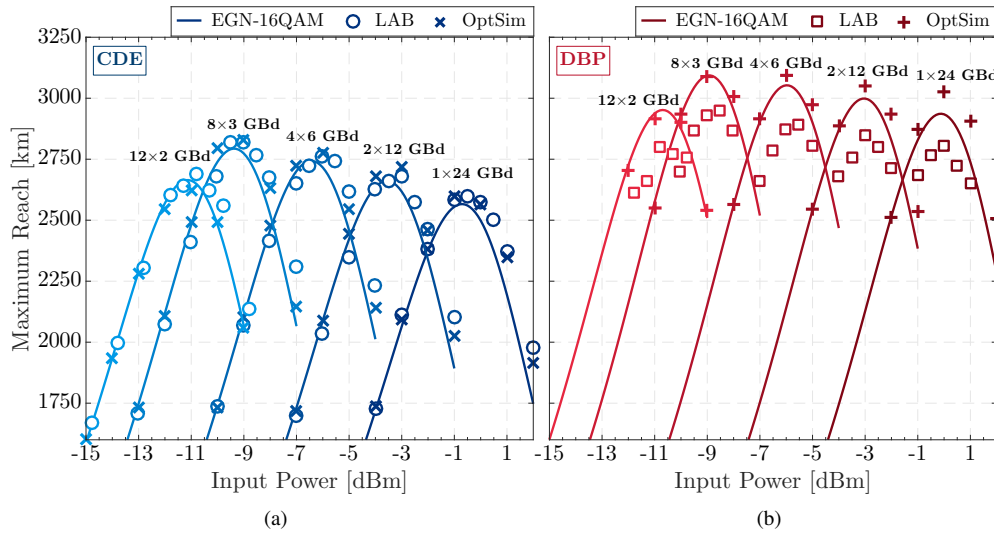
Fig. 6. Maximum reach versus input power of the SCM PM-16QAM system after SRO and/or DBP (for ease of visualization, 6×4 GBaud results are not shown).

Following this procedure, in Fig. 6 we show the achieved maximum reach by each MSC configuration after channel equalization with CDE or DBP. The experimental (LAB) and EGN results are cross validated by split-step-based simulations using the commercial software OptSim. In all cases, the second CPE stage described in section 3 is always optimized in terms of its block length. When only linear compensation is applied (CDE), an excellent agreement can be found between analytical, simulation and experimental results in Fig. 6(a). The maximum reach achieved by each MSC configuration at the corresponding optimum launch power is summarized in Fig. 7(a). The impact of symbol-rate optimization is clearly visible, reaching a peak of ∼9% for the 8 × 3 GBaud case, relatively to the baseline SC 1 × 24 GBaud. It is important to recall that, as previously discussed in section 3, the 12 × 2 GBaud MSC configuration was found to suffer from an additional 0.2 dB of B2B penalty, which translates into reach penalty as well. For consistency with the experimental conditions, this additional 0.2 dB B2B penalty was integrated both in the simulation and EGN analyses at 12 × 2 GBaud. In the simulation case, this was done through additional noise loading over the received signal, while in the EGN case we have readjusted the threshold SNR to account for the added B2B penalty, as described in equation (3). This extra B2B penalty was found to generate approximately 4% reduction in maximum reach gain through SRO, leading to a steep reach decrease at 2 GBaud, as observed in Figs. 6 and 7.

We proceed our study by assessing the performance of DBP over the MSC channel under test. To that end, we adopted a split-step Fourier method with 4 steps per span. After optimization, the nonlinear operator free parameter [20], ξ, was found to yield a stable value of $\xi \approx 0.95$. The obtained results after SCI mitigation through DBP are shown in Figs. 6(b) and 7. The EGN model results are obtained by assuming perfect cancellation of SCI. While the maximum reach gain predicted by the EGN at 1 × 24 GBaud is of ∼13%, the actual experimentally observed gain was a more modest ∼8%, even slightly lower than the SRO gain. The under-performance of DBP over experimental data has also been observed in other papers [23] and can be attributed to a set of non-ideal conditions, such as the electrical distortion introduced by the receiver and the uncertainty on the per span fiber parameters and insertion losses. Note that the recirculating loop is composed of 4 different fiber spans. The 4-5% gap between experimental DBP results and the EGN-16QAM prediction is kept almost constant across all symbol-rates. However, it
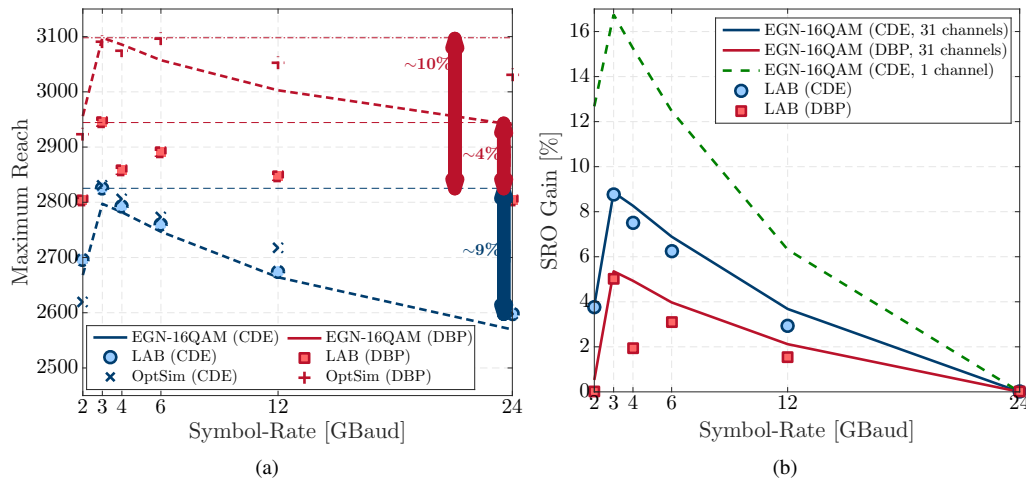
Fig. 7. a) Maximum reach at the optimum power vs symbol-rate after CDE and DBP; b) SRO gain (in %) over the baseline 1×24 GBaud MSC as predicted by the EGN model with 31 channels and single-channel input signal.

can also be noticed that the SRO effect after DBP is attenuated, both in the analytical prediction and experimental results. To investigate the reason for this SRO reduction after DBP, in Fig. 7(b) we plot the SRO gain predicted by the EGN-16QAM both in WDM (31 channels) and single-channel (SCI only) conditions. To allow for a direct comparison of the SRO effectiveness, all curves are normalized to the respective maximum reach achieved at 1×24 GBaud. It becomes apparent that a large contribution to the SRO effect comes from SCI, with a peak of ~17% at 3 GBaud. As a consequence, the partial or complete removal of SCI also removes an important contribution to the SRO effect. The peak SRO gain achieved with DBP is then reduced to about 5%, almost half of what can be expected without DBP (~9%). Taking into account the full C-band analytical results published in [6] (see Fig. 6), it is worth noting that the total WDM system bandwidth adopted in this work (~ 870 GHz) actually lies on a suboptimal region, where the NLI mitigation provided by SRO is expected to be close to its minimum. Note that, according to [6], after a minimum SRO benefit at around ~300-700 GHz of bandwidth, the NLI mitigation capabilities of SRO are expected to steadily increase as the total WDM bandwidth is widened towards full C-band. According to [6], as more channels are loaded in the system, the SRO benefit is expected to steadily increase. On the other hand, it is well known that the DBP performance will also be impacted by the addition of more channels, reducing its relative benefit in comparison with SRO [21, 22]. The results here presented can then be interpreted as providing a pessimistic overview on the achievable SRO and its relative importance in comparison with DBP, in PM-16QAM MSC systems.

It is also worth noting that the DBP performance over the simulation results is substantially more effective than the EGN-16QAM prediction at 24 GBaud (~3% difference), while it then tends to converge to EGN-16QAM maximum reach as we decrease the symbol-rate. The reason for this behavior can be related with the enhanced NLPN mitigation capability provided by the CPE with optimized block length at 24 GBaud. A closer inspection into this issue will be performed in the following section.
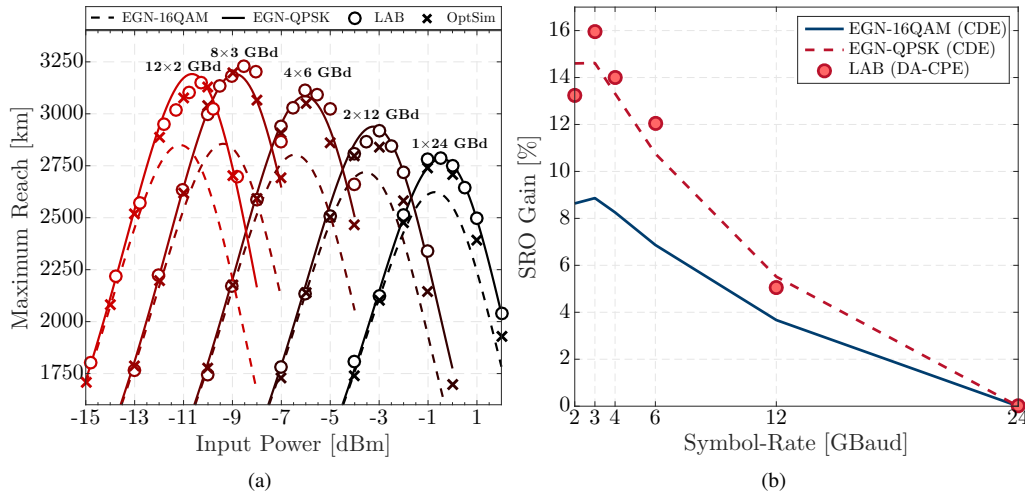
Fig. 8. Experimental, simulation and analytical results on the performance of the SCM PM-16QAM system after ideal phase noise compensation. a) Maximum reach vs input power; b) SRO vs symbol-rate.

5. Potential gains by ideal phase noise mitigation

In the previous section we have assessed the performance benefit provided by SRO in a system where phase noise is compensated by a realistic CPE with optimized block length. In previous works [19], it has been suggested that the modulation format dependence of NLI is tightly related with the NLPN phenomena. Once NLPN is fully removed, NLI appears to become essentially modulation format independent. Since it is characterized by long-term time correlation, NLPN can be partially removed by standard CPE. However, due to the high BER operation target (10^{-2}), CPE is affected by frequent errors on its data demodulation stage, which may degrade the phase noise estimation performance. The problem may become even more critical at low symbol-rate transmission, where the symbol period is larger.

To assess impact of residual phase noise in our system, we adopt a figure of merit, FOM, defined as,

$$\text{FOM} = \frac{\sum_n \text{var}\left(\text{Im}\left(C_n\right)\right)}{\sum_n \text{var}\left(\text{Re}\left(C_n\right)\right)}, \tag{4}$$

where $\text{Im}(\cdot)$ and $\text{Re}(\cdot)$ represent the real and imaginary parts of $(\cdot)$ and C_n is the n-th constellation symbol, collapsed to the origin as,

$$C_n = R_n e^{-j\angle T_n} - |T_n|, \tag{5}$$

where R_n and T_n are the complex-valued received and transmitted symbols, respectively, and $\angle(\cdot)$ denotes the angle of $(\cdot)$. Collapsing all received QAM symbols to the origin enables to map the amplitude and phase into the real and imaginary parts, respectively, of the collapsed constellation. Consequently, FOM = 1 defines a PM-16QAM constellation with perfectly circular points, whereas FOM > 1 indicates that the phase noise component is stronger than the corresponding amplitude component. On the opposite side, FOM < 1 indicates an artificial squeezing of the phase noise component over the limits of an additive white Gaussian noise channel, which can happen when using fully data-aided phase noise estimation.

With the aim to explore the performance limits of CPE, in the following we will adopt an ideal fully data-aided V&V (DA-V&V), whose block length will be adjusted to force FOM = 1.
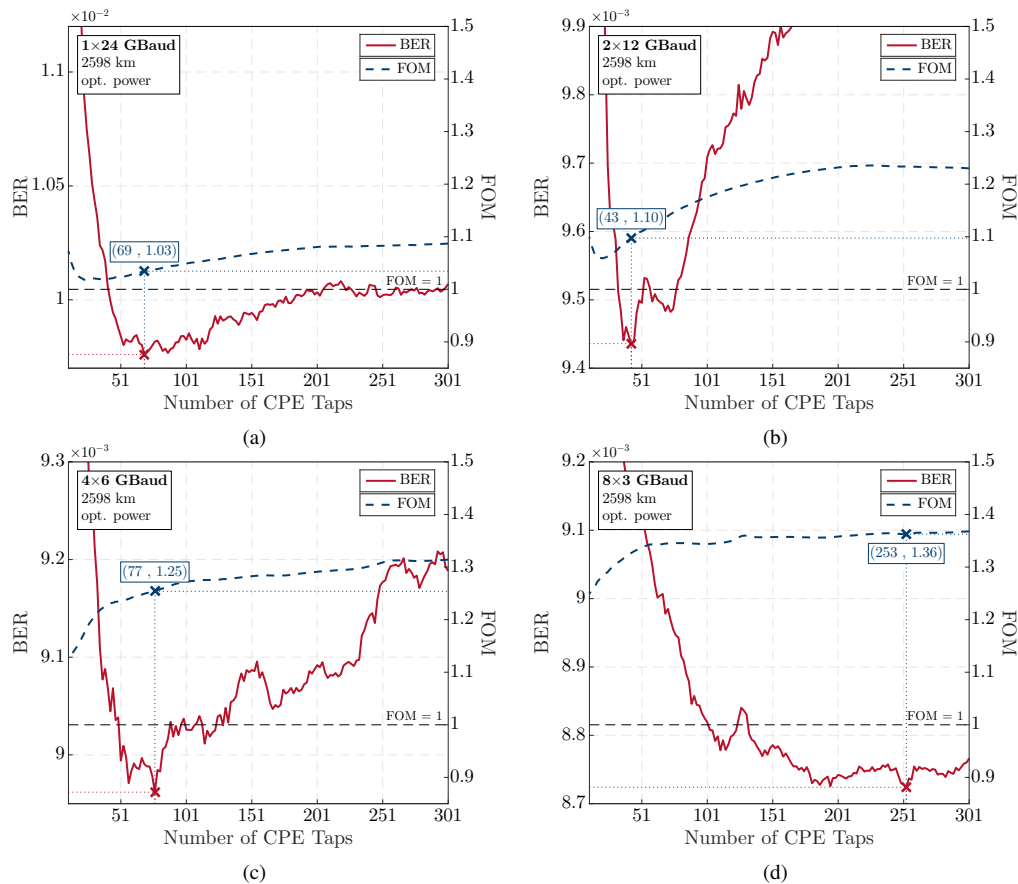
Fig. 9. Optimization of the block length of DD-V&V for phase noise mitigation after 24 spans (2598 km) and at the optimum launch power. a) 1×24 GBaud; b) 2×12 GBaud; c) 4×6 GBaud; d) 8×3 GBaud.

It is worth emphasizing the DA-V&V is addressed in this work not as a feasible option for phase noise mitigation, but rather as a benchmark of expectable performance improvement that can be achieved by an enhanced phase noise compensation algorithm. Also note that, since it operates only over the phase component, the variance of the amplitude noise is not modified by a data-aided CPE.

The maximum reach results enabled by this ideal phase processing are shown in Fig. 8(a). A good agreement was found between the simulation / experimental results and the EGN-QPSK model, corroborating the results of [19], where the EGN with QPSK correction factors was found to provide a good match with the system performance after NLPN removal. The corresponding maximum reach gain over the 1×24 GBaud configuration is shown in Fig. 8(b). It is interesting to note that the enhanced phase noise compensation enabled by the DA-V&V not only provides inherent gains in the 1×24 GBaud case (approximately 5% longer reach than the EGN-16QAM prediction, in Fig. 8(a)) but also significantly boosts SRO. Indeed, a maximum reach gain of ~15% is achieved at 3 GBaud, when the output constellation exhibits FOM = 1. It is important to refer that the B2B performance after the ideal CPE was slightly improved by 0.1 dB, now yielding a constant B2B penalty of 1 dB for all MSC configurations. This however does not change the SRO picture relatively to the 24 GBaud case (with the exception of the 12×2 GBaud
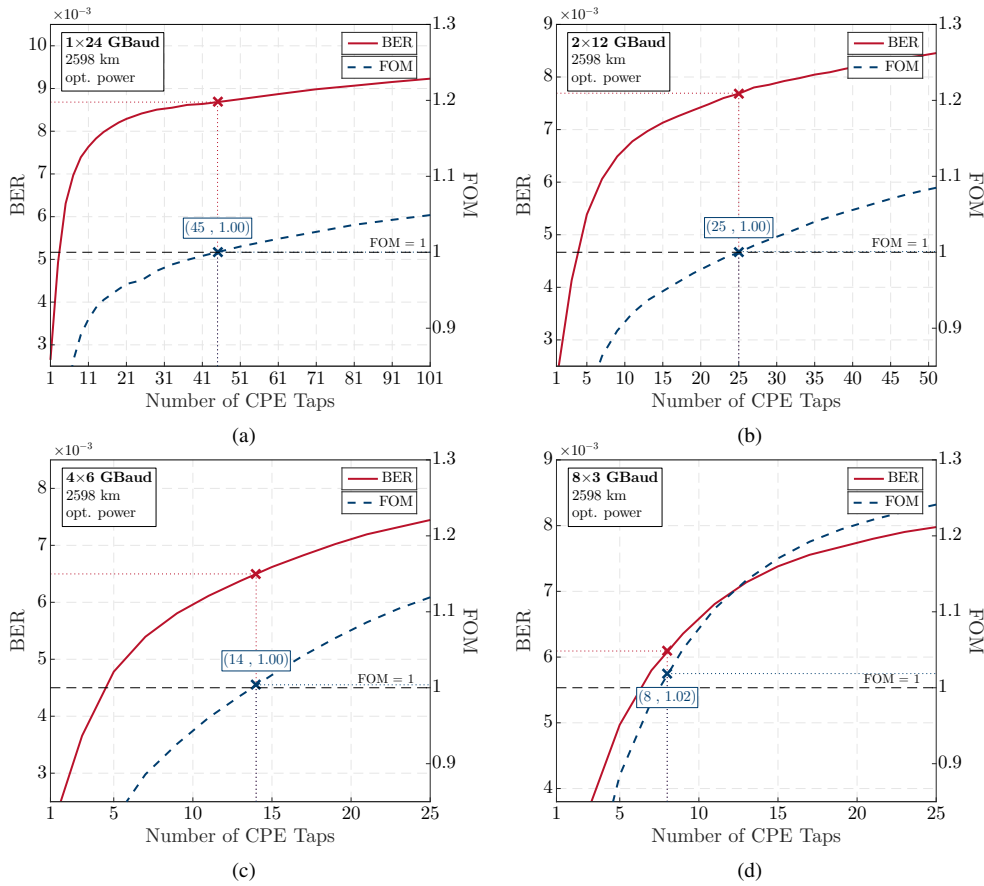
Fig. 10. Optimization of the block length of DA-V&V for phase noise mitigation after 24 spans (2598 km) and at the optimum launch power. a) 1×24 GBaud; b) 2×12 GBaud; c) 4×6 GBaud; d) 8×3 GBaud.

configuration, which is not penalized anymore).

A more detailed analysis of the FOM dependence on the symbol-rate per carrier and on the CPE optimization process is shown in Figs. 9 and 10, for the case of propagation over 24 fiber spans at the optimum power. The results are then summarized in Table 2. Note that these values have direct correspondence with the maximum reach results previously shown in Figs. 6 and 7 (CDE case) when transmission is performed over 24 fiber spans (6 recirculations) at the optimum launch power. Although DBP was not found to produce meaningful changes on the optimum number of CPE taps, the collaborative application of DBP and CPE in the presence of noise is an interesting, yet complex, problem that would require a more in-depth study. We therefore

Table 2. Optimum number of CPE taps and resulting FOM after propagation over 24 fiber spans at the optimum launch power identified in Fig. 6a.

	1×24 GBd	2×12 GBd	4×6 GBd	6×4 GBd	8×3 GBd	2×12 GBd
FOM (DD-V&V)	1.03	1.1	1.25	1.32	1.36	1.36
DD-V&V taps	69	43	77	237	253	195
DA-V&V taps	45	25	14	10	8	7

leave it for future work. Starting our analysis by the realistic decision-directed V&V (DD-V&V) employed in section 4, in Fig. 9 we observe that FOM tends to increase with decreasing symbol-rate, from 1.03 at 24 GBaud up to 1.36 at 3 GBaud. This indicates an increasing performance penalty of the DD-V&V when it is set to operate at lower symbol-rates, therefore leaving more uncompensated phase noise. In turn, the DA-V&V optimization results in Fig. 10 show that the algorithm has been controlled to yield FOM $\approx$ 1 in all cases, therefore generating output constellations with almost perfectly circular points. The number of DA-V&V taps that yields FOM $\approx$ 1 are indicated in Table 2. These can be used as an indication of the time correlation associated with the remaining phase noise (which can be partially attributed to NLPN) that is left uncompensated by the realistic DD-V&V. Note that, although the DA-V&V performance keeps on increasing for FOM < 1 (phase noise achieves a lower variance than the corresponding amplitude noise), we restrict our analysis to the case of FOM $\geq$ 1, corresponding to a realistic phase noise estimation limit in an additive white Gaussian noise channel. While at high symbol-rate the optimum number of taps of DD-V&V and DA-V&V is similar, a large discrepancy is found at lower symbol-rates. Indeed, as the symbol period is increased (lower symbol-rate) the number of DA-V&V taps is approximately proportionally decreased in order to capture a similar time window. In contrast, being unable to operate at shorter block lengths, the DD-V&V finds its optimum operation at larger number of taps, where it is more resilient to ASE noise fluctuations. Besides the considered QPSK partitioning V&V, other CPE algorithms such as blind phase search [29] and maximum likelihood phase estimation [30] have been also tested yielding similar results in terms of performance. However, a comprehensive analysis of NLPN capabilities of different CPE algorithms requires a more in-depth study that we leave as a topic for future work.

On one hand, these results highlight the difficulty of NLPN compensation through standard CPE for low symbol-rate MSC signals. On the other hand, they show promising benefits in terms of system performance, encouraging the development of enhanced NLPN mitigation schemes optimized for MSC transmission.

6. Conclusions

Through an experimental campaign on PM-16QAM MSC transmission we have demonstrated ~9% maximum reach gain through symbol-rate optimization, a similar gain to that obtained by DBP in SC transmission. Combining SRO and DBP, a peak gain of ~13% was observed over SC transmission, whereas the relative SRO was decreased to about 5% due to the partial removal of SCI. Finally, we have analyzed the impact of NLPN in the considered experimental scenario, concluding that standard CPE tends to lose its ability to compensate for NLPN at low symbol-rates. The use of an ideal phase noise compensation scheme was found to significantly enhance the SRO effect in PM-16QAM MSC transmission systems. This is an encouraging factor for the future development of enhanced NLPN mitigation algorithms for long-haul uncompensated optical links, specially when associated with MSC transmission.